Solar Energy Materials & Solar Cells 231 (2021) 111307

Contents lists available at ScienceDirect

Solar Energy Materials and Solar Cells

journal homepage: www.elsevier.com/locate/solmat

Extracting band-tail interface state densities from measurements and modelling of space charge layer resistance

Mingzhe Yu [a], Shona McNab [a], Isabel Al-Dhahir [a], Christopher E. Patrick [a], Pietro P. Altermatt [b], Ruy S. Bonilla [a,*]

[a] Department of Materials, University of Oxford, Oxford, OX1 3PH, United Kingdom
[b] Trina Solar, State Key Laboratory for Photovoltaic Science and Technology (SKL PVST), Xinbei District, Changzhou, Jiangsu Province, 213031, China

ARTICLE INFO

Keywords:
Interface state density
Dielectric surface passivation
Field-effect
Silicon-silicon dioxide interfaces

ABSTRACT

Dielectric-silicon interfaces are becoming ever more important to device performance. Charge inside a surface dielectric layer is neutralized in Si leading to an accumulation or inversion layer of free carriers. Additionally, states at the interface are occupied by charges via Shockley-Read-Hall carrier statistics. It is accepted that the density of interface charge near midgap, which can only reach a concentration as high as the density of states, D_{it}, has a minor effect on band bending compared to the charges in the dielectric for a well passivated interface. Here, we show that it is the state density near the band edge what plays the major role. We conclude this by comparing our measurements with device modelling of a Si/SiO_2 interface. We measure the wafer sheet resistance while applying various amounts of positive charge to the passivating dielectric on an n-type Si wafer, and then reproduce the measured resistance values using simulations. This modelling indicates that D_{it} at midgap has indeed a minor effect on sheet resistance change, while the total amount of tail states has a significant impact on the distribution of induced carriers. We test this model to detect the amount of acceptor-like states at the band-tails of oxide passivated silicon with different processing. We discuss and analyse the limitations of this technique. While we report on the Si/SiO_2 interface due to its relevance in photovoltaics, our method can be used to study the properties of other semiconductor-dielectric interfaces. As such this work is of importance across various optoelectronic devices.

1. Introduction

The interface defect state density is a critical property of semiconductor-dielectric interfaces. Since these states have their energy levels in the bandgap, they can therefore act as strong recombination centres or store large concentrations of charge, both of which may be detrimental to photovoltaics devices [1]. Fundamentally, these states are formed as a result of the breaking of translational symmetry when the two bulk materials are brought together to form an interface. However, the precise origin of these states and their role in device physics has been the subject of study for many decades (see Ref. [2] for a review). The states can be classified broadly as either intrinsic or extrinsic [3]. The extrinsic states require the formation of defects such as vacancies, interstitials, or impurities. These defects can create bound states whose energies depend precisely on the perturbation to the potential due to the structural and/or electronic properties of the defect [4]. In terms of device performance, extrinsic defects can give rise to localized states with energies lying towards the middle of the gap and are hence problematic [5]. These deep levels act as traps for electrons, greatly increasing the probability of recombination and decreasing the carrier density.

In the intrinsic case, terminating the periodicity of the bulk material leads to a continuum of exponentially decaying (evanescent) states whose energies lie in forbidden band gap of the bulk material. These states were first introduced in the context of metal-semiconductor junctions [6]. As indicated by the name, they are an intrinsic and fundamental property of the material. They can be understood as Bloch states of the bulk semiconductor with complex wave vector [7], and can be viewed as having valence or conduction band character depending on their energies. Often the large density of these states at the interface provides an effective mechanism to pin the Fermi level and explain the energy-level alignment at semiconductor interfaces [7]. The effect of intrinsic states on the energy levels at the interface, conveniently characterised through the density of states D_{it}, is more continuous in nature.

* Corresponding author.
E-mail address: sebastian.bonilla@materials.ox.ac.uk (R.S. Bonilla).

https://doi.org/10.1016/j.solmat.2021.111307
Received 13 May 2021; Received in revised form 5 July 2021; Accepted 27 July 2021
Available online 4 August 2021

As an illustration, consider the first-principles density-functional theory calculations of layer-resolved density-of-states for a defect-free Fe/GaAs interface as reported in Ref. [8]. They show how the interface broadens the GaAs band edges such that they form tails which decay exponentially with energy towards the middle of the gap. A more pertinent example are calculations on model Si/SiO_2 interfaces which demonstrate the evolution of the band structure as one moves between the Si and SiO_2 regions [9,10].

Altogether, the interface states have a distribution of energy at different sections of the bandgap [11], which affect interface properties in different manners. For example, there is an asymmetry in probability for capturing an electron or hole, quantified as cross-section of electron or hole capture, σ_n and σ_p respectively, in units of cm^2. Near midgap, the Coulomb interaction of charged defect states usually dominates the recombination activity in covalently bond semiconductors like silicon. Near the band edges on the other hand, the shape of the atomic orbitals often plays a significant role. Whether a defect state acts as an effective recombination centre does not only depend on its σ_n and σ_p, but also on the Shockley-Read-Hall (SRH) statistics [12,13]. For example, both an electron and a hole must be captured for recombination to happen, and the less likely carrier limits the recombination rate. In the shallow defects at the band tails the re-emission probability of one carrier is large, deeming these states often inefficient for recombination except at very high dopant density, very high injection density, or substantial band bending [12,13]. Therefore, interface states at midgap are the primary concern for achieving high surface passivation. Such midgap D_{it} continues to be intensively studied and is nowadays widely used as a metric for surface passivation [14–16].

The fundamental properties of band-tail states, on the other hand, were only studied experimentally in the 1980s and 1990s [11,17–23]. An exponential increase in density towards conduction/valence band edge was observed in such works, in agreement with theoretical calculations. A consolidation of known Si/SiO_2 interface state densities in the literature, including band tails, is shown in Fig. 1. It is clear that processing conditions can largely affect the interface properties, and that much fewer data exists for the true densities in the tails. Due to the relatively low recombination rate in such band-tail states, they have not been as prominently studied as the midgap strong recombination states. Despite this lack of attention, state density at band-tail can be several orders of magnitudes higher than that at midgap, and such band-tail states are able to store large concentrations of charge. These charges can alter the carrier distribution close to the interface via field-effect, and therefore influence surface passivation [24], and performance of devices involving a field-induced junction like inversion layer cells [25–27], metal-oxide-semiconductor field-effect transistors (MOSFETs) [28], and field-induced photodiodes [29]. The effect of band-tail state density on emitter conductivity of an inversion layer cell, and subsequently cell performance, has been evaluated and proved significant by simulations in our previous work [25]. The detection of the state density at band-tails is therefore necessary for understanding and manipulating carrier distribution at the interface, and it can point new directions for improvement of devices involving field effect.

Capacitive techniques are reliable for detection of state density at midgap, while lacking sensitivity on the states at band-tail [18,30]. Surface photovoltage can be used to acquire state density across the whole bandgap, but with compromised accuracy at band-tails where the state density varies significantly in terms of energy [18]. Electron paramagnetic resonance spectroscopy is capable of detecting the states for such defects that are paramagnetic, for example, silicon dangling bonds at the Si/SiO_2 interface [31] and the Si/SiN_x interface [32], which correspond to the states at midgap rather than at band-tails [17]. No technique has yet been developed which can quantify the band-tail states with high sensitivity. In this study, we explore the effect that interface states both at midgap and in the band-tails have on the distribution of charge-induced electrons near a Si/SiO_2 interface. Such understanding allows us to propose a novel method of extracting the interface state density at band-tails from changes in the space charge layer, with the assistance of numerical simulations.

2. Sample preparation and characterisation

Silicon wafers are used in this work with their band-tail state density characterised to demonstrate the potential of the interface characterisation method studied here. The samples start with 200 μm thick, 1 Ωcm, phosphorus-doped n-type planar float zone, (100) silicon substrates. Three set samples originate from the substrates for a diversity of interfaces. Set 1 has a 100 nm of thermal oxide grown on both sides at 1050 °C in a dry atmosphere. Some of Set 1 wafers were subsequently forming gas annealed (FGA) in 5 % hydrogen ambient at 425 °C for 30 min for enhanced chemical passivation, referred to as Set 2. Set 3 samples have a 10 nm of thermal oxide grown on both sides at 950 °C in a dry atmosphere and were annealed in 5 % hydrogen in the same way as Set 2. Fig. 2 shows the details of processing of all sets.

In order to record changes in the sheet resistance of a sample as a function of surface charge density, we apply corona discharge at 30 kV to the sample surface. This generates an electric field and induces an electron accumulation layer in silicon near the interface. The processing method and the structure of a corona charge-deposited wafer are shown in Fig. 3 a. Details on the corona discharge apparatus can be found in Refs. [34,35]. For planar Set 1 samples passivated by thermal oxide, Kelvin Probe (KP) measurements were used to acquire the surface potential of the specimen. The charge density was extracted using the formalism in Ref. [35], assuming that charge stays at the surface of the dielectric during the measurement period, which has been previously shown to be the case [34]. For textured samples with SiO_2 and SiO_2/SiN_x coatings (Set 2), monitoring the corona ion density using KP is inaccurate as the recorded contact potential difference is influenced by the

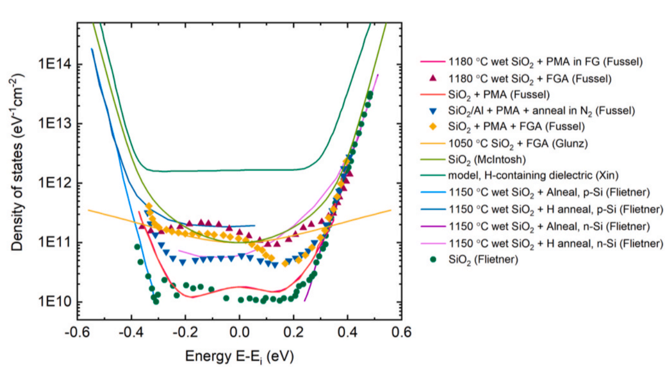

Fig. 1. Density of states distribution of various Si/SiO_2 interfaces, redrawn from Refs. [11,17,20,22,23,33]. PMA: post metallization anneal; FGA: forming gas anneal; FG: forming gas.

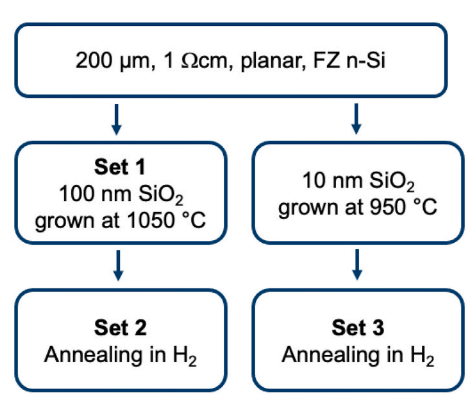

Fig. 2. Detailed processing of samples.

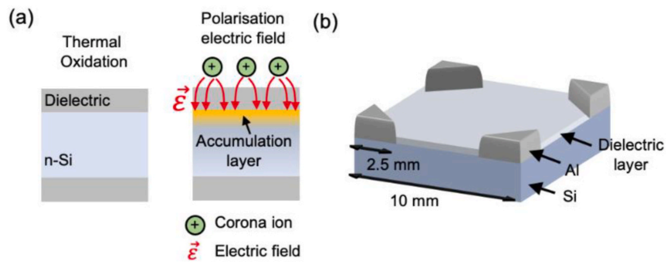

Fig. 3. (a) Processing method and schematic of a corona ion-deposited n-Si wafer. (b) Sample structure for Van der Pauw measurement.

effective surface area seen by the KP probe. The corona ion density is instead determined by the corona discharge time, with its corresponding charge density calibrated on one planar Set 1 specimen. The Van der Pauw method is used to monitor sheet resistance of a specimen [36]. Ideally, the size of contact should be infinitesimal for accurate measurement. Here we choose a contact size practical for conducting measurements and use a correction factor to compensate the influence of the contact size [37]. The sample structure is shown in Fig. 3 b. Details of the Van der Pauw measurement is included in Ref. [25]. The sample was first diced into 1 × 1 cm^2 squares, before the surface dielectric at the corners removed by a diamond scriber. A 100 nm thick aluminium was then deposited for electrical contact at the corners by masked thermal evaporation.

3. Impact of interface states on space charge layer resistance

Fig. 4 shows a schematic energy diagram of an n-Si/SiO_2 interface at an initial neutral state (a), in the presence of charged donor and acceptor interface states (b), and in the presence of dielectric charge (c, d). The conduction and valence bands are flat at the initial neutral state. When donor and acceptor interface states are considered, electrons will occupy the acceptor states below the Fermi level, accompanied by an upward band-bending. In the presence of positive dielectric charge, mirrored electrons will appear close to the interface in bulk silicon, so that the bands bend downwards, and the Fermi level moves towards the conduction band edge. This will lead to most acceptor states below the Fermi energy being filled with electrons. In the space charge region, charge-induced electrons are free carriers in bulk silicon and contribute to additional wafer conductivity. Since the proportion of trapped electrons is determined by interface state density, wafer sheet resistance can be used as a metric for finding the distribution of interface states near conduction band edge. In the presence of negative dielectric charge, the band near the interface will bend upwards. While increasing negative charge density, the Fermi level will scan across the middle part of the bandgap and then reach the band tail at valence band. This will cause holes to become the dominant carriers, occupying most of the donor states that are above the Fermi level. Hole density in the inversion layer, and therefore inversion layer conductivity, is determined by both the negative dielectric charge density and the amount of charged donor states at the interface. The interface states near valence band edge can be obtained by monitoring inversion layer sheet resistance at controlled negative charge density.

A model was developed in Sentaurus TCAD [39] to better understand the Si/SiO_2 interface, which accounts for all physical phenomena involved in the formation of the space charge layer. The model comprises a 200 μm thick, 1 Ωcm n-Si wafer, with an oxide passivation layer on both sides. Positive dielectric charge was defined at the front Si/SiO_2 interface. The interface was defined following the common parametrisation as reported in Ref. [40], with interface state densities at midgap and band tails as primary parameters. The interface defect density profile near both band edges follows an exponential dependency on energy, as shown in equations (1) and (2):

$$D_{it}(CB, acceptor) = D_{it}(max, CB, acceptor) \times e^{-\frac{(1.1-E)}{E_{CB,trap}}} \tag{1}$$

$$D_{it}(VB, donor) = D_{it}(max, VB, donor) \times e^{-\frac{E}{E_{VB,trap}}} \tag{2}$$

where $D_{it}(CB, acceptor)$ and $D_{it}(VB, donor)$ describe the acceptor/donor band-tail interface state density. $D_{it}(max, CB, acceptor)$ and $D_{it}(max, VB, donor)$ are the maximum interface state density at conduction/valence band edge, and E is the energy of the states from valence band edge in eV. $E_{CB,trap}$ and $E_{VB,trap}$ represent the slope of the tail, indicating its dependence on energy. Here $E_{CB,trap}$ has been set to 0.02 eV and $E_{VB,trap}$ to 0.024 eV to reflect average values extracted from previous works [11,17,20]. Since the energy slope and maximum states of the band tails may vary at different silicon/dielectric interfaces [41], we integrate all tail interface states into a single metric N_{it} (acceptor/donor) that describes the total amount of tail interface states available for occupation. To allow fast fitting we only vary the maximum interface state density at band edge $D_{it}(max)$, while maintaining the tail slopes, $E_{CB,trap}$ and $E_{VB,trap}$, constant. As an example, Fig. 5 shows the D_{it} distribution at Si/SiO_2 interface in a model with D_{it} (midgap) being 10^{11} $eV^{-1}cm^{-2}$, $D_{it}(max, CB, acceptor) = 10^{14}$ $eV^{-1}cm^{-2}$, and $D_{it}(max, VB, donor) = 10^{14}$ $eV^{-1}cm^{-2}$. We calculate the N_{it} (acceptor/donor) as the area under the tail, corresponding to the maximum state occupation the tail can take.

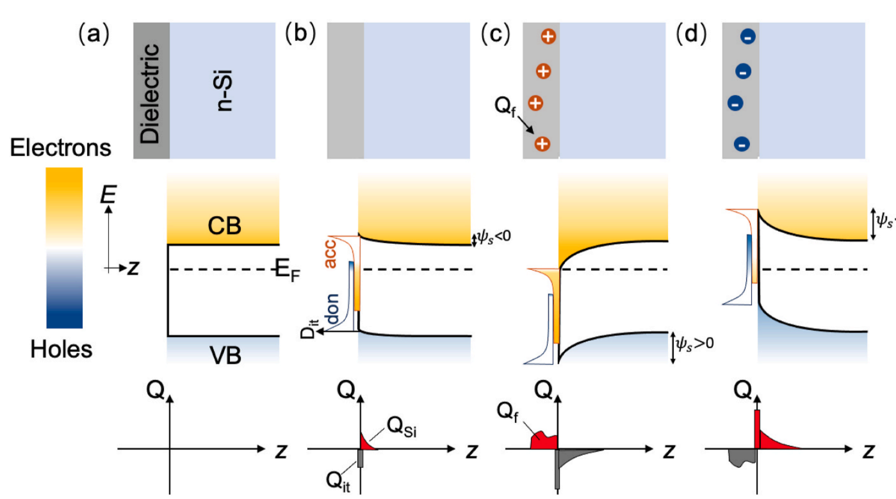

Fig. 4. Schematic energy diagram at an n-Si/SiO_2 interface at (a) an ideal neutral state, (b) in the presence of charged donor and acceptor interface states, and in the presence of (c) positive or (d) negative dielectric charge. Redrawn from Ref. [38].

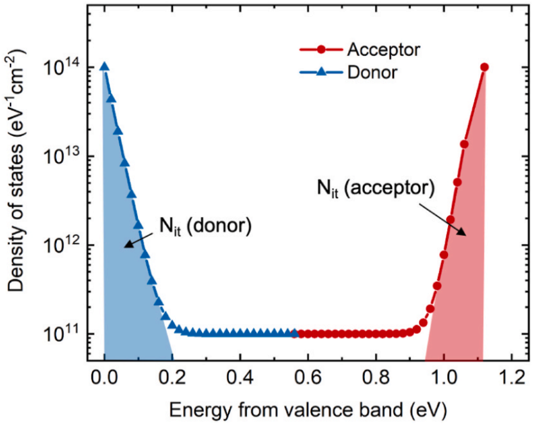

Fig. 5. Density of states distribution at Si/SiO_2 interface in a model with D_{it} being 10^{11}, 10^{14}, and 10^{14} eV^{-1}cm^{-2} at midgap, conduction band edge, and valence band edge.

N_{it} (acceptor/donor) comprehensively accounts for both the tail maximum value and its slope. In this work we will report the N_{it} (acceptor/donor) as the primary metric for characterising the impact of the tail state concentrations. The Inversion and Accumulation Layer Mobility Model (IALMob) reported for simulation of MOSFETs was used here to model the mobility throughout the sample bulk and in the space charge layer [42,43]. A density gradient quantum-mechanical model was used to account for the confined carrier distributions occurring near semiconductor–insulator interfaces [44,45]. Including these carrier density and mobility effect is critical to achieve a model that correctly reflected the measurements. The equilibrium state was then simulated, and the carrier density and mobility were extracted as a function of the distance from the Si/SiO_2 interface. Fig. 6 shows the extracted carrier density and mobility from a simulation with positive charge density of 9 $\times$ 10^{12} cm^{-2} at the front dielectric. These were then integrated over the entire sample depth to calculate the wafer sheet resistance, following equation (3):

$$R_S(wafer) = \frac{1}{\int_0^{thickness} (nq\mu_n + pq\mu_p)dt} \tag{3}$$

where n and p are electron/hole density, μ_n and μ_p are electron/hole mobility, and q is the elementary charge.

As represented in the energy diagram in Fig. 4, increasing the positive charge density will cause the Fermi level to scan across first the middle part of the bandgap, and then the band tail at conduction band edge. Wafer sheet resistance as a function of positive charge density was simulated to reflect the response of the space charge layer while introducing positive charge at the front dielectric. Since interface states at midgap and band tails can host field-induced electrons, the wafer sheet resistance vs. charge density curve was simulated for a range of D_{it} at both midgap and conduction band edge. We simulate a charge concentration up to 9 $\times$ 10^{12} q/cm^2, which approaches the practical limit of gate breakdown field in most thin film materials [46,47]. Fig. 7 shows wafer sheet resistance vs. positive charge density curves simulated from a 200 μm thick, 1 Ωcm n-Si substrate. For Fig. 7 a, the maximum D_{it} at conduction band edge is 10^{14} eV^{-1}cm^{-2}, and varied D_{it} (midgap) is applied. For Fig. 7 b, D_{it} (midgap) is 10^{11} eV^{-1}cm^{-2}, and N_{it} (acceptor) near the conduction band edge is varied. In Fig. 7 a, the change in wafer sheet resistance is less than 0.1 Ω/sq for D_{it} (midgap) below 10^{12} eV^{-1}cm^{-2}. Since this is the case for most passivated wafers [1,48], it is concluded that the variation of D_{it} (midgap) has a minor effect on local carrier distribution, and therefore on the conductivity of the space charge layer. This was expected as described in Section 1. The effect of the number of acceptor tail states, N_{it} (acceptor), is depicted in Fig. 7 b. Here it is evident that there are large changes in (i) wafer sheet

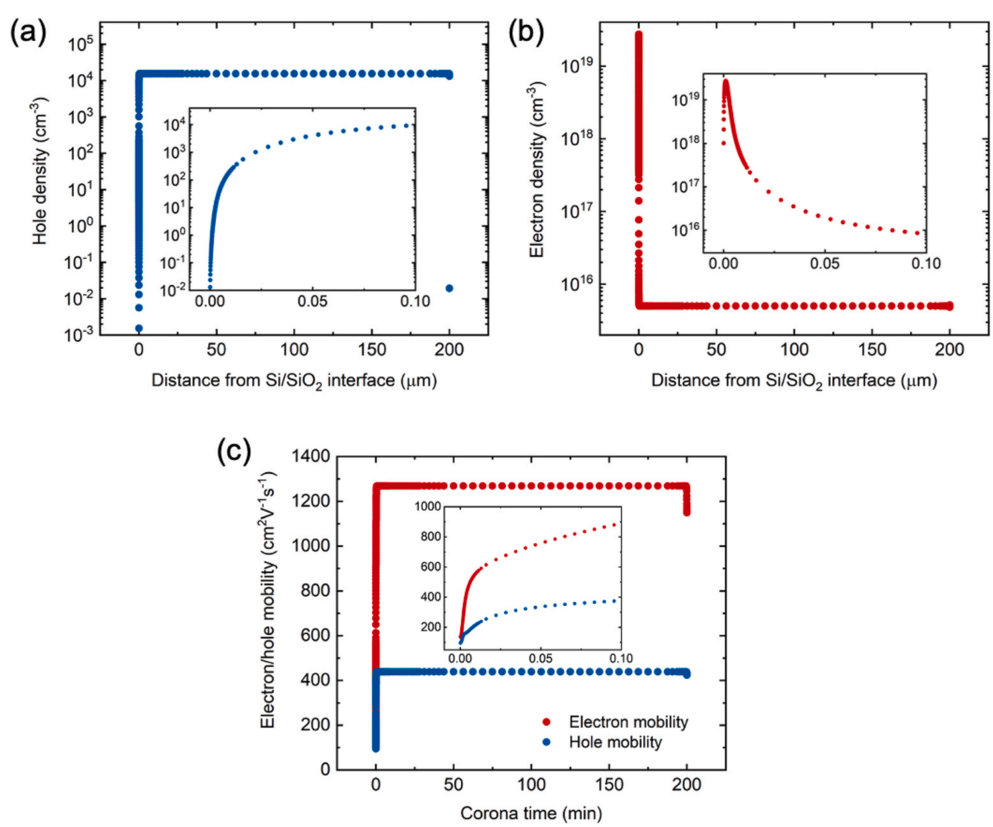

Fig. 6. Simulated carrier density, including (a) electrons and (b) holes, (c) carrier mobility across the whole wafer extracted from a n-type, 1 Ωcm model with positive charge density of 9 $\times$ 10^{12} cm^{-2} at the front dielectric. D_{it} is 10^{11}, 10^{14}, and 10^{14} eV^{-1}cm^{-2} at midgap, conduction band edge, and valence band edge.

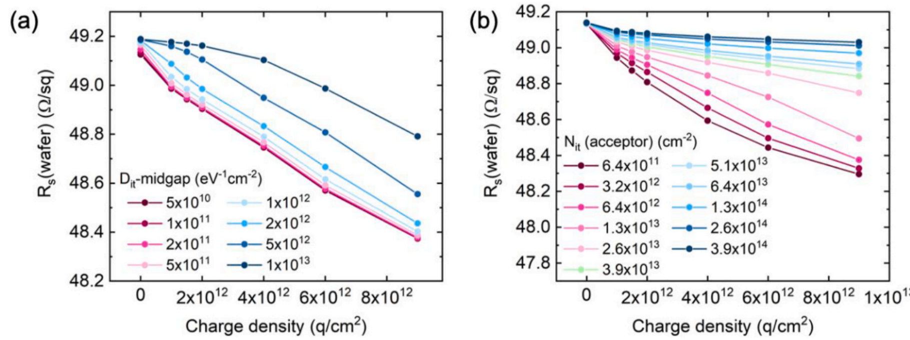

Fig. 7. Simulated wafer sheet resistance vs. positive charge density curves of a 200 μm thick, 1 Ωcm n-Si substrate at various (a) D_{it} (midgap), and (b) N_{it} (acceptor) near conduction band edge.

resistance and (ii) the dependence of resistance on positive surface charge density. The wafer sheet resistance vs. positive charge density curve is therefore useful for determining the distribution of interface states, especially for those near the conduction band edge.

We also evaluate the potential of the method to detect the amount of donor tail states near valence band edge, N_{it} (donor). An inversion layer sheet resistance as a function of negative charge density was simulated from the same 200 μm thick, 1 Ωcm n-Si substrate. Fig. 8 shows the inversion layer sheet resistance vs. negative charge density with varied N_{it} (donor), for charge concentrations up to 9×10^{12} cm^{-2}. D_{it} (midgap) is set to 10^{11} $eV^{-1}cm^{-2}$. The thickness of the inversion layer is determined by where the electron density exceeds that of holes. The effect of N_{it} (donor) is shown in Fig. 8. Similar to the effect of N_{it} (acceptor) in Fig. 7 b, large changes are observed in (i) inversion layer sheet resistance, and (ii) the dependence of resistance on negative surface charge density. The parameters used to describe the model are listed in Table 1. Based on the analysis above, measurements of R_s in combination with simulations make it possible to detect both the acceptor and donor tail states.

4. Method for extraction of interface properties

We developed a method to extract N_{it} (acceptor) of an n-type specimen from a combination of measurements and simulation. First, we acquire a wafer sheet resistance vs. positive charge density curve of a passivated silicon wafer by recording the wafer sheet resistance while introducing controlled amounts of positive corona charges to the sample surface. A series of wafer sheet resistance vs. positive charge density curves are then generated by simulations with fine adjustments of wafer resistivity and N_{it} (acceptor) to fit the experimental curve. The combination of wafer resistivity and N_{it} (acceptor) generating the best fitting curve are extracted for the specimen. Examples of N_{it} (acceptor) extraction are given in Section 5.

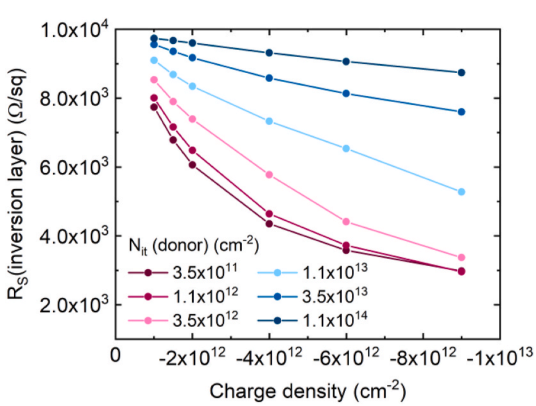

Fig. 8. Simulated inversion layer sheet resistance vs. negative charge density of a 200 μm thick, 1 Ωcm n-Si substrate at various N_{it} (donor) near valence band edge.

Table 1
Summary of parameters used for simulation of wafer sheet resistance in the presence of dielectric charge in Sentaurus TCAD.

Parameter	Value
Wafer thickness	200 μm
Bulk base resistivity	n-type, 0.96–1.04 Ωcm
SRH bulk lifetime	$\tau_n = 0.371$ ms, $\tau_p = 3.71$ ms
Dielectric charge density	$-9x10^{12}$ - 9×10^{12} cm^{-2}
D_{it} (midgap)	5×10^{10} - 10^{13} $eV^{-1}cm^{-2}$
D_{it} (max, band tail)	CB: 10^{13} – 6×10^{15} $eV^{-1}cm^{-2}$ VB: 10^{13} – 3×10^{15} $eV^{-1}cm^{-2}$

Fitting between the simulated and experimental data is determined by two metrics: (i) the wafer sheet resistance, which can shift the curve in the y-axis, and (ii) the slope of the curve at high charge densities (2–9 $\times 10^{12}$ cm^{-2}), which reflects the dependence of wafer sheet resistance on positive charge density. The reliability of this method is evaluated here by calculating the slope of the 2–9 $\times 10^{12}$ cm^{-2} range of the curve as a function of N_{it} (acceptor). Fig. 9 shows the curves extracted from simulations on a 200 μm thick, 1 Ωcm n-Si substrate. In Fig. 9 a, D_{it} (midgap) is 10^{11} $eV^{-1}cm^{-2}$ and N_{it} (donor) is 3.54×10^{12} cm^{-2}. Fig. 9 a shows the change in slope as a function of N_{it} (acceptor), with the slope being more sensitive at lower N_{it} (acceptor). For N_{it} (acceptor) below 10^{13} $eV^{-1}cm^{-2}$, the amount of interface states to accommodate the induced electrons is too low to be differentiated by monitoring wafer sheet resistance. This method is therefore not applicable for N_{it} (acceptor) below 10^{13} $eV^{-1}cm^{-2}$. Wafer resistivity is also varied to show its effect on the simulated dependence. Here it is clear that a change of wafer resistivity by 0.04 Ωcm will cause an evident shift of the curve, meaning that the wafer resistivity has to be precise in the model for an accurate extraction of N_{it} (acceptor). Since the non-uniformity in wafer resistivity is unavoidable even across a same wafer, along with the slope, the simulated and experimental R_s-Q relations require fitting in y-axis for correct base resistance, and subsequent extraction of N_{it} (acceptor). D_{it} (midgap) is varied in Fig. 9 b where it is clear that it has almost no effect on the curve. Therefore, interface states at midgap does not affect extraction of N_{it} (acceptor) with this method. According to the analysis above, N_{it} (acceptor) can be extracted with this method with no evident artifacts originating from wafer resistivity variations, or variation in D_{it} (midgap).

To extract N_{it} (donor), we need to measure sheet resistance of an inversion layer. It is to note that inversion layer could not be contacted using the sample structure in Fig. 3 b. This is because of the discontinuity in inversion layer underneath the Aluminium patches, which can be solved by local doping. Due to the lack of local doping tools in our laboratory, the method to extract N_{it} (donor) is not evaluated in this work.

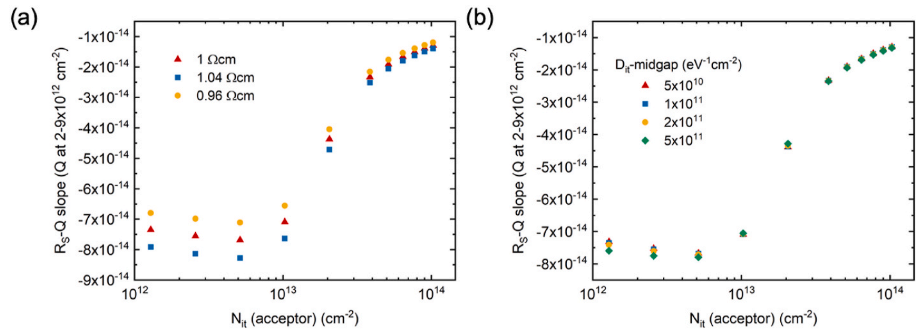

Fig. 9. Slope of simulated wafer sheet resistance vs. positive charge density curve on a 200 μm thick, 1 Ωcm n-Si substrate at charge density in the range of 2–9 × 10^{12} cm^{-2}, as a function of N_{it} (acceptor), with varied (a) wafer resistivity, and (b) D_{it} (midgap).

5. Extraction of interface properties

The amount of acceptor band-tail states of the samples described in Section 2 is extracted to demonstrate the potential of this characterisation method. Wafer sheet resistance as a function of positive charge density was recorded as shown in the symbols in Fig. 10 a. Wafer resistivity and N_{it} (acceptor) at the Si/SiO_2 interface were then adjusted in the numerical model. The best fit for each sample is shown as a solid line, and the parameters obtained are listed in Table 2. The extracted N_{it} (acceptor) values for each set are compared in Fig. 10 b, and are found in agreement with data reported in Refs. [11,17,20,38]. It is to note that the lowest N_{it} (acceptor) reported for Set 1 (100 nm oxide) and Set 3 (10 nm oxide, FGA) are at the lower end of the detection limit observed in Fig. 9. When extracting the R_s-Q_f slope from the experimental data, the model would seem to require lower N_{it} (acceptor) to fit the slope more accurately. This condition appears to be due to the mobility model chosen here (IALMob). This model has been mainly tested in MOSFETs that use base dopant density of the order of $>10^{16}$ cm^{-3} [42,43], while a typical dopant density in this work is 5 × 10^{15} cm^{-3}. Better accuracy in extracting N_{it} (acceptor) would hence require a tested model of accumulation and inversion layer carrier mobility for dopant densities commonly used in PV devices. In Fig. 10 b, no evident drop in N_{it} (acceptor) is observed for the Si/SiO_2 (100 nm) sample after an FGA, indicating that the enhanced chemical passivation by FGA is not evident at the band tail. For the two sets with FGA, the set with 10 nm of oxide presents lower N_{it} (acceptor) values than the one with 100 nm of oxide, which may originate from the difference in oxidation temperature (1050 °C for 100 nm vs. 950 °C for 10 nm specimens). Sheet resistance vs. charge density measurements on Set 1 samples were conducted after an IPA rinse to check for possible degradation as a result of corona discharge. These showed that no substantial change occurs in the band-tail states, and are included in the supplementary materials.

Overall, these results corroborate the fact that interface states not only act as recombination centres for photo-generated carriers, but also accommodate substantial charge and thus affect local carrier density. Interface states are therefore important for surface architectures based on band bending, for example, field-effect passivation, inversion layer cells, MOSFETs, and field-induced photodiodes. The characterisation technique studied in this work is shown to allow sensitive detection of interface states at band tails and it is therefore of importance across various interfaces in optoelectronic devices. However, here we highlight the limitation of this technique as follows: (i) this method is losses accuracy for N_{it} (acceptor/donor) below 10^{13} eV^{-1}cm^{-2}, (ii) detection of N_{it} under inversion conditions is only possible with additional processing of local doping under the contacts, and (iii) better accuracy of the technique requires a tested model of accumulation and inversion layer carrier mobility for dopant densities commonly used in PV devices. In addition, electrical quality of the dielectric is to be controlled to avoid accuracy limitation of the technique by leakage from the film. The leakage can be monitored and characterised using Kelvin Probe. Provided these limitations are consider carefully this technique can help understand the effect of band tails on the performance of optoelectronic devices.

6. Conclusions

At a semiconductor-dielectric system, the concentration of charge-induced carriers and therefore conductivity of the induced layer is dependent on dielectric charge density and interface state density. This work explores the potential to extract interface state density near both band edges from measurements of induced layer conductivity at controlled charge density with the aid of simulations. Simulations of wafer sheet resistance vs. positive charge density show changes in D_{it} (midgap) at the n-Si/SiO_2 interface have a minor effect on the carrier densities at the interface. On the other hand, changes in N_{it} (acceptor) cause a remarkable shift in both the wafer sheet resistance and the

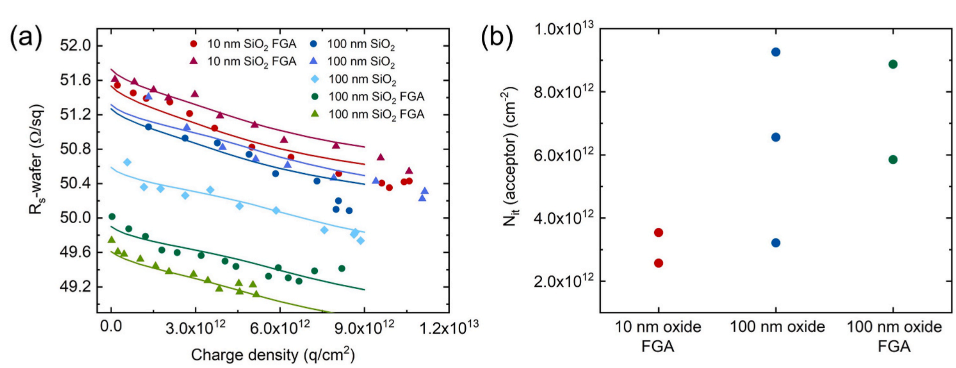

Fig. 10. (a) Experimental (symbols) and simulated (lines) wafer sheet resistance vs. positive charge density curves, and (b) extracted N_{it} (acceptor) for each set of samples.

Table 2
Details of parameters used in simulations for best fits with experimental wafer sheet resistance vs. charge density curves of each set of samples.

	10 nm oxide, FGA		100 nm oxide			100 nm oxide, FGA	
	Sample 1	**Sample 2**	**Sample 1**	**Sample 2**	**Sample 3**	**Sample 1**	**Sample 2**
Wafer resistivity	1.053	1.049	1.045	1.044	1.03	1.016	1.01
D_{it} (max, CB, acceptor)	5.5×10^{13}	$<4 \times 10^{13}$	1.02×10^{14}	$<5 \times 10^{13}$	1.44×10^{14}	1.38×10^{14}	9.1×10^{13}
N_{it} (acceptor)	3.54×10^{12}	$<2.57 \times 10^{12}$	6.56×10^{12}	$<3.21 \times 10^{12}$	9.26×10^{12}	8.87×10^{12}	5.85×10^{12}

dependence of wafer sheet resistance to surface charge density. Such feature was found key in extracting the N_{it} (acceptor) from measurements. Simulation results show that the technique reduces in accuracy for N_{it} (acceptor/donor) above 10^{13} $eV^{-1}cm^{-2}$. Similar effects were observed for N_{it} (donor) via simulating inversion layer sheet resistance in the presence of negative charge, showing the possibility of extracting both N_{it} (acceptor) and N_{it} (donor) with this method. However, additional local doping processing is required for the detection under inversion conditions. Examples of utilising this technique indicates that a tested model of accumulation and inversion layer carrier mobility model for dopant densities commonly used in PV devices is required for better accuracy of the detection. The sensitive detection of N_{it} (acceptor), and potentially that of N_{it} (donor) makes this method a powerful complement to current interface characterisation techniques. The technique can therefore provide insight in understanding and manipulating of carrier distribution at semiconductor–dielectric interfaces, and point to strategies for improvement.

CRediT authorship contribution statement

Mingzhe Yu: Investigation, Validation, Methodology, simulation, Writing – original draft. **Shona McNab:** Investigation. **Isabel Al-Dhahir:** Investigation. **Christopher E. Patrick:** Validation, Writing – original draft. **Pietro P. Altermatt:** Validation, Methodology, Writing – original draft. **Ruy S. Bonilla:** Conceptualization, Methodology, Software, Writing – original draft, Supervision.

Declaration of competing interest

The authors declare that they have no known competing financial interests or personal relationships that could have appeared to influence the work reported in this paper.

Acknowledgements

All authors are thankful to Radka Chakalova for assistance in cleanroom processing. M. Yu would like to thank the China Scholarship Council for funding her doctoral studies. P.P. Altermatt acknowledge support from Black Silicon Photovoltaics grant EP/R005303/1. R. S. Bonilla was supported by the Royal Academy of Engineering under the Research Fellowship scheme and acknowledges the support from the EPSRC Postdoctoral Fellowship EP/M022196/1.

Appendix A. Supplementary data

Supplementary data to this article can be found online at https://doi.org/10.1016/j.solmat.2021.111307.

References

[1] A.G. Aberle, Crystalline Silicon Solar Cells : Advanced Surface Passivation and Analysis, Centre for Photovoltaic Engineering, University of New South Wales, Sydney, 2009.
[2] J.F. Wager, K. Kuhn, Device physics modeling of surfaces and interfaces from an induced gap state perspective, Crit. Rev. Solid State Mater. Sci. 42 (2017) 373–415, https://doi.org/10.1080/10408436.2016.1223013.
[3] J. Robertson, Band offsets of wide-band-gap oxides and implications for future electronic devices, J. Vac. Sci. \& Technol. B Microelectron. Nanom. Struct. Process. Meas. Phenom. 18 (2000) 1785–1791, https://doi.org/10.1116/1.591472.
[4] C. Freysoldt, B. Grabowski, T. Hickel, J. Neugebauer, G. Kresse, A. Janotti, C.G. de Walle, First-principles calculations for point defects in solids, Rev. Mod. Phys. 86 (2014) 253–305, https://doi.org/10.1103/RevModPhys.86.253.
[5] H. Feichtinger, Deep centers in semiconductors, in: Handb. Semicond. Technol., John Wiley & Sons, Ltd, 2000, pp. 167–229, https://doi.org/10.1002/9783527621842.ch4.
[6] V. Heine, Theory of surface states, Phys. Rev. 138 (1965) A1689–A1696, https://doi.org/10.1103/PhysRev.138.A1689.
[7] J. Tersoff, Schottky barrier heights and the continuum of gap states, Phys. Rev. Lett. 52 (1984) 465–468, https://doi.org/10.1103/PhysRevLett.52.465.
[8] T. Iffländer, S. Rolf-Pissarczyk, L. Winking, R.G. Ulbrich, A. Al-Zubi, S. Blügel, M. Wenderoth, Local density of states at metal-semiconductor interfaces: an atomic scale study, Phys. Rev. Lett. 114 (2015) 146804, https://doi.org/10.1103/PhysRevLett.114.146804.
[9] F. Giustino, A. Pasquarello, Electronic and dielectric properties of a suboxide interlayer at the silicon–oxide interface in MOS devices, Surf. Sci. 586 (2005) 183–191, https://doi.org/10.1016/j.susc.2005.05.012.
[10] S. Markov, P. Sushko, C. Fiegna, E. Sangiorgi, A. Shluger, A. Asenov, From ab initio properties of the Si-SiO2 interface, to electrical characteristics of metal-oxide-semiconductor devices, J. Phys. Conf. Ser. 242 (2010) 12010, https://doi.org/10.1088/1742-6596/242/1/012010.
[11] H. Flietner, W. Füssel, N.D. Sinh, H. Angermann, Density of states and relaxation spectra of etched, H-terminated and naturally oxidized Si-surfaces and the accompanied defects, Appl. Surf. Sci. 104–105 (1996) 342–348, https://doi.org/10.1016/S0169-4332(96)00168-7.
[12] W. Shockley, W.T. Read, Statistics of the recombinations of holes and electrons, Phys. Rev. 87 (1952) 835–842, https://doi.org/10.1103/PhysRev.87.835.
[13] R.N. Hall, Electron-hole recombination in germanium, Phys. Rev. 87 (1952) 387, https://doi.org/10.1103/PhysRev.87.387.
[14] R.S. Bonilla, B. Hoex, P. Hamer, P.R. Wilshaw, Dielectric surface passivation for silicon solar cells: a review, Phys. Status Solidi Appl. Mater. Sci. 214 (2017) 1–30, https://doi.org/10.1002/pssa.201700293.
[15] J. Schmidt, R. Peibst, R. Brendel, Surface passivation of crystalline silicon solar cells: present and future, Sol. Energy Mater. Sol. Cells. 187 (2018) 39–54, https://doi.org/10.1016/j.solmat.2018.06.047.
[16] S.W. Glunz, F. Feldmann, SiO2 surface passivation layers – a key technology for silicon solar cells, Sol. Energy Mater. Sol. Cells. 185 (2018) 260–269, https://doi.org/10.1016/j.solmat.2018.04.029.
[17] H. Flietner, U-Shaped distributions at semiconductor interfaces and the nature of the related defect centres, Phys. Status Solidi. 91 (1985) 153–164, https://doi.org/10.1002/pssa.2210910120.
[18] Y.W. Lam, E.H. Rhoderick, Surface-state density and surface potential in MIS capacitors by surface photovoltage measurements. II, J. Phys. D. Appl. Phys. 4 (1971) 1376–1389, https://doi.org/10.1088/0022-3727/4/9/319.
[19] H. Flietner, Spectrum and nature of defects at interfaces of semiconductors with predominant homopolar bonding, Surf. Sci. 200 (1988) 463–471, https://doi.org/10.1016/0039-6028(88)90553-5.
[20] W. Füssel, M. Schmidt, H. Angermann, G. Mende, H. Flietner, Defects at the Si/SiO2 interface: their nature and behaviour in technological processes and stress, Nucl. Instruments Methods Phys. Res. Sect. A Accel. Spectrometers, Detect. Assoc. Equip. 377 (1996) 177–183, https://doi.org/10.1016/0168-9002(96)00205-7.
[21] M.H. Cohen, M.Y. Chou, E.N. Economou, S. John, C.M. Soukoulis, Band tails, path integrals, instantons, polarons, and all that, IBM J. Res. Dev. 32 (1988) 82–92, https://doi.org/10.1147/rd.321.0082.
[22] S.W. Glunz, D. Biro, S. Rein, W. Warta, Field-effect passivation of the SiO2-Si interface, J. Appl. Phys. 86 (1999) 683–691, https://doi.org/10.1063/1.370784.
[23] K.R. McIntosh, S.C. Baker-Finch, N.E. Grant, A.F. Thomson, S. Singh, I.D. Baikie, Charge density in atmospheric pressure chemical vapor deposition TiO2 on SiO2-passivated silicon, J. Electrochem. Soc. 156 (2009) G190, https://doi.org/10.1149/1.3216029.
[24] R.S. Bonilla, K. Collett, L. Rands, G. Martins, R. Lobo, P.R. Wilshaw, Stable, extrinsic, field effect passivation for back contact silicon solar cells, Solid State Phenom 242 (2015) 67–72. https://doi.org/10.4028/www.scientific.net/SSP.242.67.
[25] M. Yu, Y. Shi, J. Deru, I. Al-Dhahir, S. McNab, D. Chen, M. Voss, E.-T. Hwu, A. Ciesla, B. Hallam, P. Hamer, P.P. Altermatt, P. Wilshaw, R.S. Bonilla, Assessing the potential of inversion layer solar cells based on highly charged dielectric nanolayers, Phys. Status Solidi – Rapid Res. Lett. n/a (2021), https://doi.org/10.1002/pssr.202100129.
[26] F. Werner, J. Schmidt, Manipulating the negative fixed charge density at the c-Si/Al 2O3 interface, Appl. Phys. Lett. 104 (2014), https://doi.org/10.1063/1.4867652.

[27] R. Har-Lavan, D. Cahen, 40 years of inversion layer solar cells: from MOS to conducting polymer/inorganic hybrids, IEEE J. Photovoltaics 3 (2013) 1443–1459, https://doi.org/10.1109/JPHOTOV.2013.2270347.
[28] J.J. Liou, A. Ortiz-Conde, F. Garcia-Sanchez, MOSFET physics and modeling, in: Anal. Des. Mosfets Model. Simul. Param. Extr., Springer US, Boston, MA, 1998, pp. 1–108, https://doi.org/10.1007/978-1-4615-5415-8_1.
[29] M.A. Juntunen, J. Heinonen, V. Vähänissi, P. Repo, D. Valluru, H. Savin, Near-unity quantum efficiency of broadband black silicon photodiodes with an induced junction, Nat. Photonics 10 (2016) 777–781, https://doi.org/10.1038/nphoton.2016.226.
[30] C.N. Berglund, Surface states at steam-grown silicon-silicon dioxide interfaces, IEEE Trans. Ele. ED- 13 (1966) 701–705, https://doi.org/10.1080/10408437308245838.
[31] C.R. Helms, E.H. Poindexter, The silicon-silicon dioxide system: its microstructure and imperfections, Reports Prog. Phys. 57 (1994) 791–852, https://doi.org/10.1088/0034-4885/57/8/002.
[32] D. Jousse, J. Kanicki, J.H. Stathis, Observation of multiple silicon dangling bond configurations in silicon nitride, Appl. Phys. Lett. 54 (1989) 1043–1045, https://doi.org/10.1063/1.101558.
[33] Z. Xin, S. Duttagupta, M. Tang, Z. Qiu, B. Liao, A.G. Aberle, R. Stangl, An improved methodology for extracting the interface defect density of passivated silicon solar cells, IEEE J. Photovoltaics. 6 (2016) 1080–1089, https://doi.org/10.1109/JPHOTOV.2016.2576685.
[34] R.S. Bonilla, C. Reichel, M. Hermle, P. Hamer, P.R.P.R. Wilshaw, Long term stability of c-Si surface passivation using corona charged SiO2, Appl. Surf. Sci. 412 (2017) 657–667, https://doi.org/10.1016/j.apsusc.2017.03.204.
[35] R.S. Bonilla, N. Jennison, D. Clayton-Warwick, K.A. Collett, L. Rands, P. R. Wilshaw, Corona charge in SiO2: kinetics and surface passivation for high efficiency silicon solar cells, Energy Procedia 92 (2016) 326–335, https://doi.org/10.1016/j.egypro.2016.07.090.
[36] L.J. van der Pauw, A method of measuring specific resistivity and Hall effect of discs of arbitrary shape, Philips Res. Reports. 13 (1958) 1–9.
[37] R. Chwang, B.J. Smith, C.R. Crowell, Contact size effects on the van der Pauw method for resistivity and Hall coefficient measurement, Solid State Electron 17 (1974) 1217–1227, https://doi.org/10.1016/0038-1101(74)90001-X.
[38] R.S. Bonilla, I. Al-dhahir, M. Yu, P. Hamer, P.P. Altermatt, Charge fluctuations at the Si – SiO 2 interface and its effect on surface recombination in solar cells, Sol. Energy Mater. Sol. Cells. 215 (2020) 110649, https://doi.org/10.1016/j.solmat.2020.110649.
[39] Synopsys, Sentaurus device, (n.d.). https://www.synopsys.com/silicon/tcad/device-simulation/sentaurus-device.html (accessed April 29, 2021)..
[40] S.W. Glunz, S. Rein, J. Knobloch, W. Wettling, T. Abe, Comparison of boron- and gallium-doped p-type Czochralski silicon for photovoltaic application, Prog. Photovoltaics Res. Appl. 7 (1999) 463–469, https://doi.org/10.1002/(SICI)1099-159X(199911/12)7:6<463::AID-PIP293>3.0.CO;2-H.
[41] R.A. Street, Hydrogenated Amorphous Silicon, 1991, https://doi.org/10.1017/cbo9780511525247.
[42] Syed Aon Mujtaba, Advanced Mobility Models for Design and Simulation of Deep Submicrometer Mosfets, Thesis, 1995.
[43] M.N. Darwish, J.L. Lentz, M.R. Pinto, P.M. Zeitzoff, T.J. Krutsick, H.H. Vuong, An improved electron and hole mobility model for general purpose device simulation, IEEE Trans. Electron Devices. 44 (1997) 1529–1538, https://doi.org/10.1109/16.622611.
[44] M.G. Ancona, H.F. Tiersten, Macroscopic physics of the silicon inversion layer, Phys. Rev. B. 35 (1987) 7959–7965, https://doi.org/10.1103/PhysRevB.35.7959.
[45] M.G. Ancona, G.J. Iafrate, Quantum correction to the equation of state of an electron gas in a semiconductor, Phys. Rev. B. 39 (1989) 9536–9540, https://doi.org/10.1103/PhysRevB.39.9536.
[46] H. Bartzsch, D. Glöß, P. Frach, M. Gittner, E. Schultheiß, W. Brode, J. Hartung, Electrical insulation properties of sputter-deposited SiO2, Si3N4 and Al2O3 films at room temperature and 400 °C, Phys. Status Solidi. 206 (2009) 514–519, https://doi.org/10.1002/pssa.200880481.
[47] V. Leonov, C. Van Hoof, M. Goedbloed, R. Van Schaijk, Charge injection and storage in single-layer and multilayer inorganic electrets based on SiO2 and Si3N4, IEEE Trans. Dielectr. Electr. Insul. 19 (2012) 1253–1260, https://doi.org/10.1109/TDEI.2012.6259999.
[48] A.G. Aberle, Surface passivation of crystalline silicon solar cells: a review, Prog. Photovoltaics Res. Appl. 8 (2000) 473–487, https://doi.org/10.1007/978-3-319-75377-5_8.